

# Opto-electronic properties of $WS_2$

Paweł Palczyński

September 11, 2018

## Declaration

## Acknowledgements

## Abstract

## List of abbreviations

## List of figures

## List of tables

## 1 Introduction

Following the discovery and characterisation of graphene in last decade the focus has been put on other 2D materials. Similar to graphene other bulk layered materials can exist in a monolayer or few layer form. Furthermore these thin layers also exhibit a significant change of properties when number of layers decreases from bulk all the way to monolayer. One of the most popular groups of these materials are transition metal dichalcogenides (TMDC). Their general form is  $MX_2$  where M is a transition metal, and X is a chalcogen atom.

### 1.1 Properties of TMDCs

TMDCs in their layered form have been known, studied and utilised for a long time. They can be found commonly in use as solid-state lubricants or catalysts. About 60 different TMDCs have been studied and characterised with a general formula of X-M-X where a plane of metal atoms (M) is sandwiched between two chalcogen planes (X). Out of those 40 can be considered layered materials where individual layers are strongly bonded in-plane and weakly bonded out-of-plane in between layers. These weak, interlayer, Van der Waals interactions allow to form a bulk material. These bonds are also what allows for those layers to slide on top of one another similarly to other layered materials like graphite. TMDCs consist of two transition metal and single chalcogen atoms covalently bonded. They can be found in 3 distinct structural polytypes: 1T (tetragonal symmetry, octahedral coordination) with single layer per repeat unit, 2H (hexagonal symmetry,

trigonal prismatic coordination) with 2 layers per repeat unit and 3R (rhombohedral symmetry, trigonal prismatic coordination) with 3 layers per repeat unit [42] as can be seen in Figure 1.

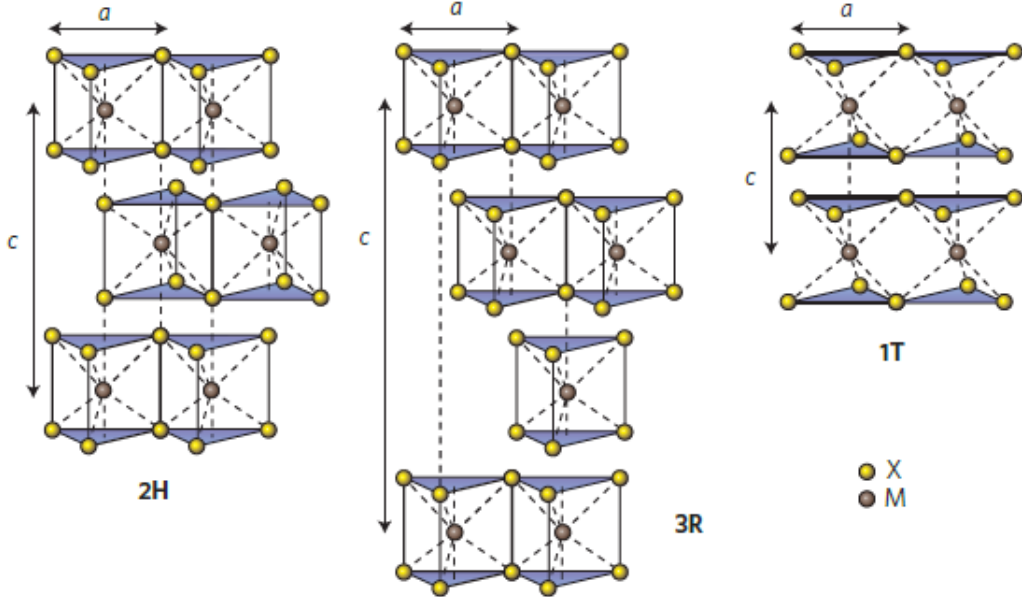


Figure 1: Schematics of the structural polytypes: 2H (hexagonal symmetry, two layers per repeat unit, trigonal prismatic coordination), 3R (rhombohedral symmetry, three layers per repeat unit, trigonal prismatic coordination) and 1T (tetragonal symmetry, one layer per repeat unit, octahedral coordination). The chalcogen atoms (X) are yellow and the metal atoms (M) are grey. The lattice constants  $a$  are in the range 3.1 to 3.7 Å for different materials. Adopted from [42]

Since graphene have proven to be difficult to work with in the fields of semiconductors due to its lack of natural finite electronic band gap its role as a successor in electronic and opto-electronic devices remains to be seen. However the techniques learned and effects observed during its characterisation were easily transferred to other layered compounds such as TMDCs. In particular the semiconducting, group VI-based TMDCs, containing sulphur and selenium as chalcogen atoms have proven to be more readily potentially useful as an active material in electronic and opto-electronic devices. This is due to their inherent electronic and optical bandgap in visible-near IR range.

As the number of layers changes from bulk to monolayer the properties of the TMDC undergo a significant change. In most TMDCs the bandgap changes from indirect to a larger direct one.

## 1.2 Electronic properties

One of the most interesting features that the layered TMDC materials exhibit is the shift in the bandstructure with the changing number of layers. Several studies have shown in simulations and experimentally that TMDCs have very similar electronic band structure as seen in example of  $WS_2$  in Figure 2. In bulk  $WS_2$  the maximum of the valence band (VBM) at  $\Gamma$  point and the minimum of the conduction band (CBM) at  $\Lambda$  form an indirect bandgap. As the number of the layers decreases the CBM at  $\Lambda$  point as well as VBM at  $K$  point increases causing the band gap to widen. At 2 layers the  $K$  point becomes the actual CBM and a new indirect bandgap forms between  $\Gamma$  point and  $K$  point. Finally in a  $WS_2$  monolayer the VBM at  $K$  point as well as entire conduction

band increases to form a new greater direct band gap at  $K$  point. This means that  $WS_2$  bandgap changes from 1.3 eV indirect bandgap in bulk to 2.1 eV direct bandgap in monolayer.

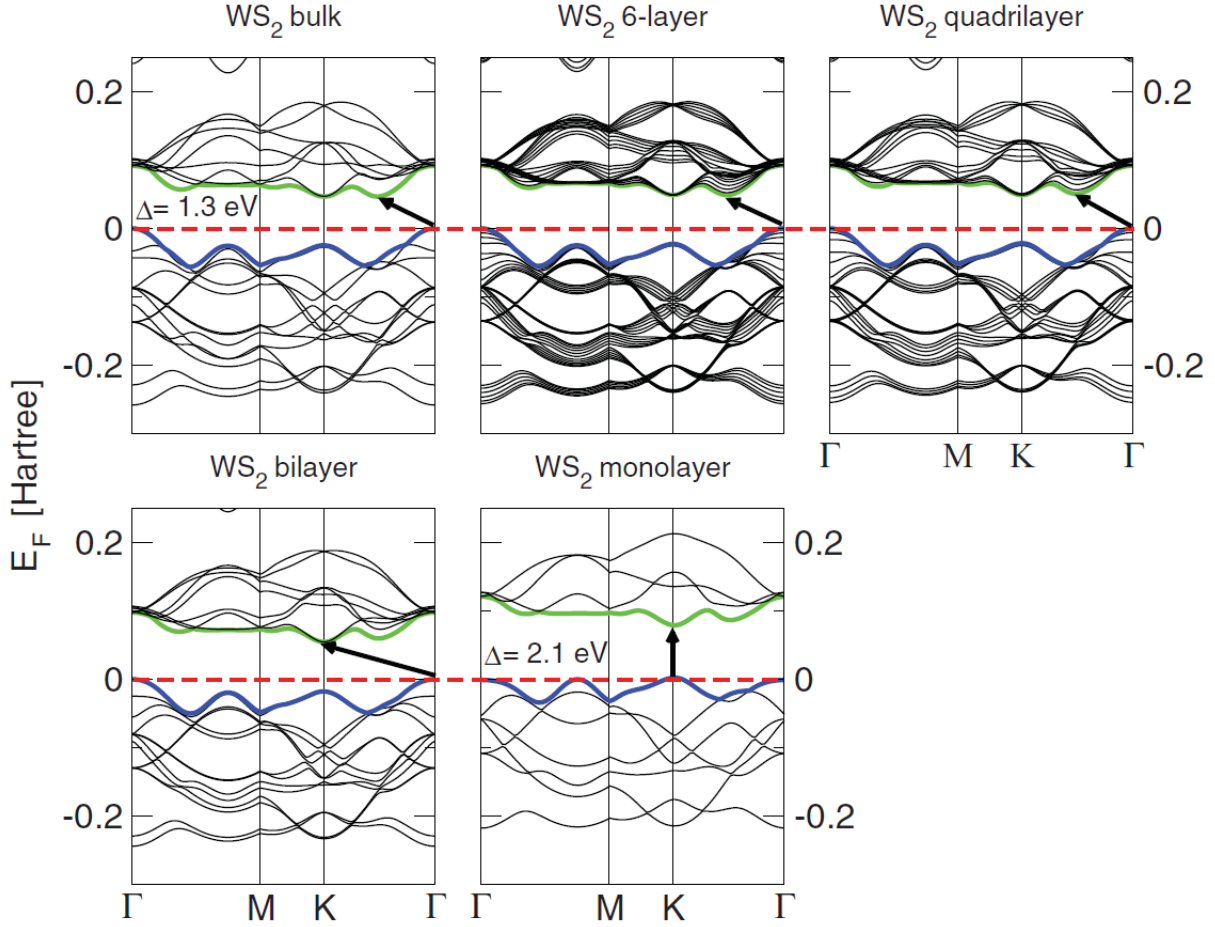


Figure 2: Band structures of bulk  $WS_2$ , its monolayer, as well as, polylayers calculated from the density functional theory (DFT) simulation. The horizontal dashed lines indicate the Fermi level. The arrows indicate the fundamental band gap (direct or indirect) for a given system. The top of valence band (blue) and bottom of conduction band (green) are highlighted. Adopted from Ref. [21]

Like  $WS_2$  other Mo and W based TMDC undergo similar transitions as seen in Table 1. In all cases the smaller indirect bandgap changes to greater direct bandgap with monolayer bandgap ranging from 1.1 eV to about 2.1 eV. Moreover the VBM at  $K$  points exhibits the orbit-spin band splitting at the  $K$  point of about 400 meV. This direct bandgap leads to presence of A and B excitons generated by transition between CBM and two VBM at the  $K$  point. The conduction band as well as the valence band are dominated by the d-electron orbitals of the transition metal atoms and at the VBM and CBM they hybridize with the p-electron orbitals of the chalcogenide atoms. Because the hybridization happens mostly at the  $\Gamma$  point and the chalcogenide atoms are at the surface of the TMDC layer it leads to strong interactions between the layers. This leads to significant change in the band structure at the  $\Gamma$  and rise of the indirect bandgap as a result of increased number of layers. On the other hand at the  $K$  point the d-orbitals of the transition metals remain mostly unaffected due to them being positioned in the middle of the layer [21] [39]

Table 1: Mo and W based TMDC bandgaps comparison

M\X	$-S_2$	$-Se_2$	$-Te_2$
Mo	Semiconducting	Semiconducting	Semiconducting
	1L: 1.8 eV	1L: 1.5 eV	1L: 1.1 eV
	Bulk: 1.2 eV	Bulk: 1.1 eV	Bulk: 1.0 eV
W	Semiconducting	Semiconducting	Semiconducting
	1L: 2.1 eV	1L: 1.7 eV	1L: 1.1 eV
	Bulk: 1.4 eV	Bulk: 1.2 eV	

### 1.3 Optical properties

TMDCs exhibit a wide array of opto-electronic effects due to their strong light-matter effects. These effects are mostly caused by the abundant presence of excitons, bi-excitons, trions or bound excitons. As a result the change in layer thickness from bulk to monolayer alters the photoluminescence, photoconductivity and absorption in the visible to infrared range.

The primary and most common quasi-particle that forms in such system is an exciton, which is a pair of a negatively charged electron and a positively charged hole bound together by Coulomb forces to form a structure similar to that of hydrogen atom. Such pair is electrically neutral and is of size exceeding size of single cell which makes it a Wannier–Mott exciton. The recombination of these excitons results in a photon emission which can be easily observed during photoluminescence characterisation. On top of excitons other quasi-particles such as trions, bi-excitons or bound excitons can be found. A trion is a group of 2 electrons and a hole or 2 holes and an electron, or otherwise described as a charged exciton. The exact nature of the trion depends usually on the type of intrinsic doping of the TMDC. A bi-exciton is a pair of excitons which is usually only observed in quantum dot systems but can be also seen in excitonically dense systems such as TMDCs. A bound exciton is similar to the free exciton but is trapped by a defect. In a typical photoluminescence spectrum several peaks can be observed depending on specific type of TMDC characterised. In  $WS_2$  monolayer for instance as seen in Figure. 3 the strongest peak (often labelled as an A peak) at about 1.97 eV is caused by the direct transition of single-photon generated exciton. Slightly redshifted by about 30 meV from the A peak a generally weaker peak caused by the trion recombination can be found. At higher energies another peak can be observed due to the presence of bi-excitons. At around the 1.3 eV a much weaker peak (I) can be seen caused by the indirect transition. Additionally a B peak can be observed blueshifted from the A peak which is caused by valley splitting as discussed in chapter 1.2. As seen in Figure 3 as the number of layers increases the main A peak becomes dramatically weaker due to lack of direct transition and redshifted following the pattern discussed in chapter 1.2. At the same time the I peak becomes relatively stronger and eventually dominates the bulk material.

Figure 3: Typical PL spectra of  $WS_2$

Similarly the photoconductivity of the TMDCs is strongly reliant on the number of layers and incident photon energy. The  $MoS_2$  for instance shows 3 times stronger photoconductivity in monolayer around 1.8 eV, where the direct transition is located, than in 2L  $MoS_2$  around 1.6 eV.

Additionally the photoconductivity appears to increase in steps with relation to the photon energy following the direct and indirect transitions. [42].

The sunlight absorption in TMDCs has been shown to be significantly more intense than in commonly used solar cell materials, at about 5-10% which is an order of magnitude greater compared to similar thickness of Si or GaAs. It is also stronger compared to 2-3% of sunlight absorption of graphene. As a result a excitonic solar cell based on  $MoS_2/WS_2$  bilayer shows about 1% power efficiency, about 3 times greater than that of typical ultrathin solar cells [2].

During standard single photon excitation photoluminescence studies the excitons generated can be called "bright" since they appear in PL spectrum. The reason we can observe them easily is because the spin between an electron and a hole is conserved, and thus allowing for photon emission. However another combination is possible, called dark exciton, where both electron and the hole have the same spin. Because of that they cannot recombine by emitting a photon and therefore remain absent from the PL spectrum. Even though they exist much longer than their bright counterparts their presence is of course also more difficult to observe. One way to observe them is to use two photon excitation. Due to two photon selection rule the single photon excitation can be excluded and the dark excitonic states can be observed. In  $WS_2$  the dark excitons result in two peaks at 2.28 eV and 2.48 eV. [Probing excitonic dark states in single-layer tungsten disulphide]

Defect engineering allows to tune the number of charge carriers. In  $MoS_2$  or  $WS_2$  the sulfur vacancies lead to increased number of electrons in the material. Because of that by increasing the number of defects in those materials the level of n-doping can be changed. An easy way to observe the presence of those defects and subsequent quenching of them is to expose the material to varying amounts of oxygen, nitrogen or water. Due to greater electronegativity (???) those species attract the electrons and therefore the electron population in the material decreases. This in turn leads to smaller trion population since trions require an extra electron to form. This then can be observed in PL as a more narrow direct peak, with especially smaller redshifted shoulder. The effect can also be of course reversed by decreasing the amount of oxygen, nitrogen or water in the environment since those exist in already in ambient conditions [Optical control of charged exciton states in tungsten disulfide].

In order to introduce and control the amount of vacancies in the TMDC different method have to be explored. One of the ways of achieving that in already grown material is the use of oxygen plasma. It has been shown that the number of defects can be controlled by limiting the plasma exposure. During the process the oxygen also chemically bonds to the  $MoS_2$  at the defect sites and therefore partially negates the effect of defects on the optical properties. The PL can also be seen to increase in intensity with increasing number of defects with oxygen adsorbed due to the increased yield of bound excitons localised at these defects. [Strong Photoluminescence Enhancement of  $MoS_2$  through Defect Engineering and Oxygen Bonding]

Similar effect has been shown using the 2,3,5,6-tetrafluoro-7,7,8,8-tetracyanoquinodimethane ( $F_4TCNQ$ ), 7,7,8,8-tetracyanoquinodimethane ( $TCNQ$ ) and (nicotinamide adenine dinucleotide)  $NADH$  for chemical doping. Both  $F_4TCNQ$  and  $TCNQ$  are p-type dopants while  $NADH$  is a n-type dopant. By exposing the surface of  $MoS_2$  to these compounds the change in PL intensity and FWHM have been observed. Similar to doping with  $O_2$ ,  $N_2$  or  $H_2O$ , all of which are p-type dopants, the intensity of PL has increased in presence of  $F_4TCNQ$  and  $TCNQ$ . The effect has been similarly ascribed to lowering the number of defects and therefore the lowering the trion population and subsequently increasing the exciton population increasing the yield. The opposite observation has been made with use of  $NADH$  with PL intensity decreasing. Similarly the increase in trion population with lower PL yield is ascribed to the lower PL intensity. [Tunable Photoluminescence of Monolayer  $MoS_2$  via Chemical Doping].

It has also been shown that alloying can be used to fine tune the PL by varying the concentration of alloying material. In monolayer  $Mo_{1-x}W_xS_2$  the PL peak position initially decreases from 1.575 eV (PL peak position of pure MoS<sub>2</sub>) to 1.56 eV at x=0.21 and then increase up to 1.65 eV (PL peak position of WSe<sub>2</sub>) at x = 1. This effect could be attributed to the linearity of VB and non-linearity of CB with regards to change in W composition. The PL position can therefore be engineered on a monotonic range from 1.56 eV to 1.65 eV. In bilayer  $Mo_{1-x}W_xS_2$  alloy the position of both direct and indirect transition PL peaks increases monotonically from about 1.49 eV and 1.53 eV for pure MoSe<sub>2</sub> to 1.56 eV and 1.62 eV for pure WSe<sub>2</sub> as the W amount is increased. This opens another relatively easy way of engineering PL position [Two-Dimensional Molybdenum Tungsten Diselenide Alloys: Photoluminescence, Raman Scattering, and Electrical Transport].

Another effect that has been demonstrated that allows for certain degree of control of PL in TMDCs is relation between the helicity of incident light and valley population valley population. It has been shown that by exciting the monolayer  $MoS_2$  with right-polarised light the resulting excitons will fill primarily the VB at K point. Similarly by exciting the  $MoS_2$  with left-polarised light the excitons will fill the VB at K' point. After recombination the resulting photons will exhibit the same circular polarity as the photons that excited the electrons in the first place. [Tightly bound trions in monolayer MoS<sub>2</sub>] [Control of valley polarization in monolayer MoS<sub>2</sub> by optical helicity]

The temperature effect on TMDCs has also been investigated. In  $WSe_2$  monolayer it has been shown that as the temperature of the sample increases from room temperature to about 400K the position of the direct transition PL peak redshifts from about 1.65 eV to about 1.58 eV. When the temperature is decreased from room temperature to about 5K the same peak blueshifts to about 1.7 eV. Between 100K and 50K as well 20K and 5K the position of the PL peak does not change. Additionally around 120K another peak appears and as the temperature is lowered it also blueshifts although less than the RT peak. The peak only present at RT is attributed to free excitons whereas the peak appearing at 120K is ascribed to bound excitons. As bound exciton peak appears its intensity increases with lower temperature while the intensity of the free exiton peak decreases. This indicates that the population of free excitons decreases while the population of the bound excitons increases with decreasing temperature [40]

There has been many reports on the spatial distribution of PL in the TMDCs. One of the observed patterns in WS<sub>2</sub> and MoS<sub>2</sub> has been that of much stronger PL intensity at the edges of the flakes. That effect has been primarily observed in small flakes of about 5  $\mu m$  [12].

## 1.4 Phonon dispersion

The vibrational and phononic characteristics of TMDCs have been investigated at length by both theoretical simulations as well as experimental studies. The  $2H - MX_2$  crystal structure of the TMDCs belongs to  $D_{6h}^4$  point group and there are 18 lattice dynamical modes at the  $\Gamma$  point. Phonons belonging to these modes can be represented as Eq. 1 [43]:

$$\Gamma = A_{1g} + 2A_{2u} + B_{1u} + 2B_{2g} + E_{1g} + 2E_{1u} + E_{2u} + 2E_{2g} \quad (1)$$

In TMDCs 4 active Raman modes can be observed  $E_{1g}$ ,  $E_{2g}^1$ ,  $E_{2g}^2$ ,  $A_{1g}$ . These can be seen in Figure 4. The  $E_{2g}^2$  is a shear mode that involves 2 layers vibrating against each other. The  $E_{1g}$  is an in-plane vibration of chalcogen atoms but is forbidden in the back-scattering configuration. For monolayers therefore it leaves primarily the  $E_{2g}^1$  which is an in-plane mode involving vibration of both metal and chalcogen atoms as well as  $A_{1g}$  which is an out-of-plane mode involving only chalcogen atoms.

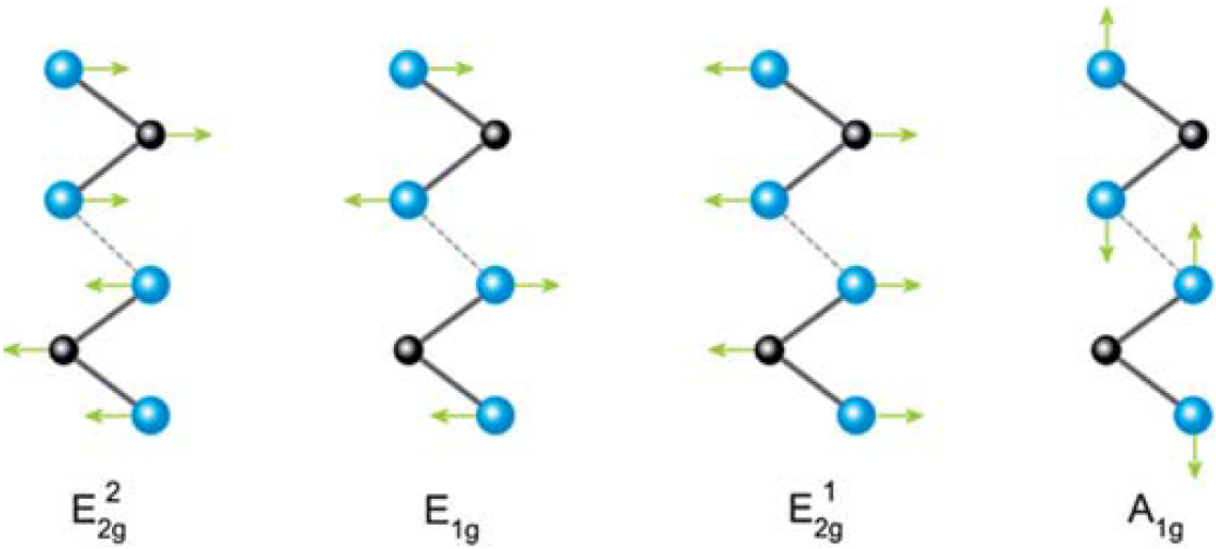


Figure 4: 4 active Raman modes in TMDCs. Metal atoms and chalcogen atoms are black and blue respectively. Adopted from [43]

These two peaks tend to dominate the spectrum of any TMDCs, whether monolayer or few-layer or bulk. The shear mode  $E_{2g}^2$  appears at low Raman shift frequencies and is therefore difficult to observe but can be used to differentiate monolayer from few-layer material. Since  $E_{2g}^1$  is an in-plane mode it tends to be unaffected by the number of layers due to weak van der Waals forces between the layers but can be seen to be slightly redshifted as the number of layers increases. As seen in Figure 5 the  $E_{2g}^1$  peak at about  $352\text{ cm}^{-1}$  is overlapping with another stronger peak, a 2LA(M) peak at  $350\text{ cm}^{-1}$  which is a longitudinal acoustic mode caused by in-plane collective oscillations of W and S atoms. The second strongest peak at around  $416\text{ cm}^{-1}$  is an  $A_{1g}$  peak, caused by out of plane vibrations. Because of that it is much more sensitive to the number of layers and is seen to become blueshifted as the number of layers increases. This has been attributed to the restorative forces as well as increase in dielectric screening of the Coulomb forces. Combining both of these shifts in frequency with the changing number of layers the difference between these two peak position can be used to identify the number of layers in TMDCs as seen in Figure 6

Figure 5: Typical Raman spectrum of  $WS_2$

Figure 6: Identification of number of layers by the difference in position of  $A_{1g}$  and  $E_{2g}^1$  peaks.

## 1.5 Heterostructures

## 1.6 Applications

# 2 Methods

### 2.1 Raman spectroscopy theory

### 2.2 Photoluminescence spectroscopy theory

### 2.3 XPS theory

## 3 Role of precursors in growth of monolayer $WS_2$

In this chapter the CVD growth of  $WS_2$  using different precursors is investigated. The as grown samples were characterised by Raman and PL spectroscopy as well as XPS, XRD, AFM and electrical measurements. As a result it was concluded that using  $H_2WO_4 + NaCl$  at 850 °C gives best results. Such grown samples exhibit biggest flakes up to 200  $\mu m$  in size as well as show the strongest and most narrow PL peak with 36 meV FWHM. The samples grown using  $H_2WO_4 + NaCl$  at 950 °C show also best transistor electron mobility in monolayer CVD grown  $WS_2$  while that grown using  $WO_3 + NaCl$  at 950 °C shows best transistor electron mobility in bilayer CVD grown  $WS_2$ .

### 3.1 Introduction

Monolayers of transition metal sulphides and selenides exhibit range of interesting properties such as strong light absorption in the IR and visible range [31][2][53], valley polarisation [30] [15], spin-orbit interactions [47][54], tightly bound excitons [29] or second-harmonic generation [25]. Some of these effects can be attributed to the lack of free dangling bonds and configuration of d-orbitals [44], [24].

Among these materials one of the most promising is the  $WS_2$ . Its visible range bandgap of 2eV as well as an easy and safe manufacturing route via CVD makes it one of the more interesting and studied TMDCs. The typical characterisation by photoluminescence spectroscopy allows to probe the varying synthesis conditions, the grain boundaries or defect population [12] [34] [23] [37]. The PL efficiency in as-grown monolayer  $WS_2$  produced via CVD growth shows ~2-6% efficiency [34][49] [26]. This efficiency is caused mostly by defect-mediated non-radiative recombination centres [1]. LEDs have been successfully produced [18] showing external quantum efficiency up to 10% [51][45].  $WS_2$  is typically a n-type semiconductor due to the presence of sulphur vacancies [12][38][17]. In order to utilise this material in any potential future applications a reliable and scalable manufacturing method must be developed to ensure a high quality crystal on the wafer scale area. The main method for  $WS_2$  synthesis that satisfies these conditions is Chemical Vapour Deposition (CVD) [13]. The growth of tungsten based TMDCs have been less successful than the equivalent molybdenum based TMDCs and has produced mostly isolated flakes of up to 40  $\mu m$  [12] [52] [37] [7][48][8][22]. Even larger films of monolayer  $WS_2$  have been shown, however they also exhibit low carrier mobility [19][9]. In the typical CVD synthesis process the sulphur and tungsten oxide are evaporated simultaneously in a tubular furnace with a constant flow of carrier gas like argon at temperatures of at least 900 °C [12][52][37][7][48][8][22]. Such growth is predi-

cated by topotactic transformation leading to low density distribution of domains on an amorphous [12][52][7][8][22] or crystalline substrate [37][48][33] possibly due to low evaporation rates of  $WO_3$ . Since  $WO_3$  requires high temperatures of 950-1000 °C to evaporate while the  $S$  becomes volatile at 90 °C the thermodynamics of the process are difficult to control. The low growth dictated by fast evaporation of  $S$  leads to limited domain growth and lack of continuous layer. One of the proposed solutions have been to spread the  $WO_3$  on the target substrate [34][23][9][5][50][11][10]. This has however led to low reproducibility, poor control of thickness and stoichiometry and unreacted material left on the substrate. Another approach has been to use more volatile  $W$  precursors such as  $WCl_6$ [3] or  $W(CO)_6$ [19][6] together with organic compounds as  $S$  precursors. Such method while producing a large area domains at lower temperature has led to lower crystal quality and purity.

Here we propose a different method of CVD synthesis that allows for much larger flake growth of up to 800  $\mu m$  at temperature of 750 degreeC. Such grown material exhibits high electron mobility in one and two layers of  $WS_2$ , higher than other values reported in literature. The photoluminescence peak is also very narrow at 36 meV FWHM at room temperature.

### 3.2 Results

For the purpose of comparing the CVD synthesis method conditions the several sets of precursors were used:  $WO_3$ ,  $WO_3 + NaCl$  and  $H_2WO_4 + NaCl$ . The standard growth procedure involves two separate crucibles placed at distance from each other in a quartz tube. Each of these crucibles is independently heated to ensure that the  $S$  and the  $W$  precursors evaporation rate is maximised at the same time. The vapours then are deposited on  $SiO_2/Si$  (285 nm) substrate which is placed close to the  $W$  precursor crucible. The entire process is performed under low vacuum and a supply of Ar gas. By following this method a reproducible deposition of large area flakes can be shown. As seen in Figure 7 the size of the flakes increases from left to right as the precursors used ( $WO_3$ ,  $WO_3 - NaCl$  and  $H_2WO_4 - NaCl$ ) change as well as demonstrating the lower temperature required to achieve these growths. All of these growths result in formation of triangular flakes with sharp edges and uniformity of colour throughout which suggest a high quality, pristine material across the flake. The growth using only  $WO_3$  results in formation of small flakes of 10  $\mu m$  at 950 °C while no growth occurs at lower temperatures (Figure 7). This can be explained by the high sublimation temperature of  $WO_3$ .

The growth can also be observed using  $WO_3 + NaCl$  at 950 °C and 850 °C with the former showing flakes of size of about 60  $\mu m$  while the latter showing smaller flakes of about 30  $\mu m$  in size. To explain this difference in size a Robinson & Robin model can be used which states that at higher temperatures the diffusivity of the adsorbed precursors is favourable to the expansion of the existing domains. On the other hand the desorption of the adsorbed species is high leading which limits the supersaturation and formation of new domains. If the temperature is lowered even further to 750 °C then no growth is observed at all, most likely due to slow evaporation of  $WO_3$  precursor.

With the change of precursors from  $WO_3$  to  $H_2WO_4$  a signifacnt change in size of flakes is observed at 850 °C and higher temperatures with lengths exceeding 200  $\mu m$ . Additionally the growth have been shown to occur at 750 °C with flakes of the size of 50-200  $\mu m$ . Moreover continuous monolayer areas of up to 0.8 mm in size has been shown (Figure 16). By increasing the growth pressure (1.6 mbar to 13 mbar) at 950 °C bilayer  $WS_2$  flakes can be preferentially formed (Figure 17).

By replacing  $WO_3$  with  $H_2WO_4$  the lateral size of the  $WS_2$  monolayered domains significantly increases (Figure 1g,h,i). The triangular crystals have edge lengths exceeding 200  $\mu m$

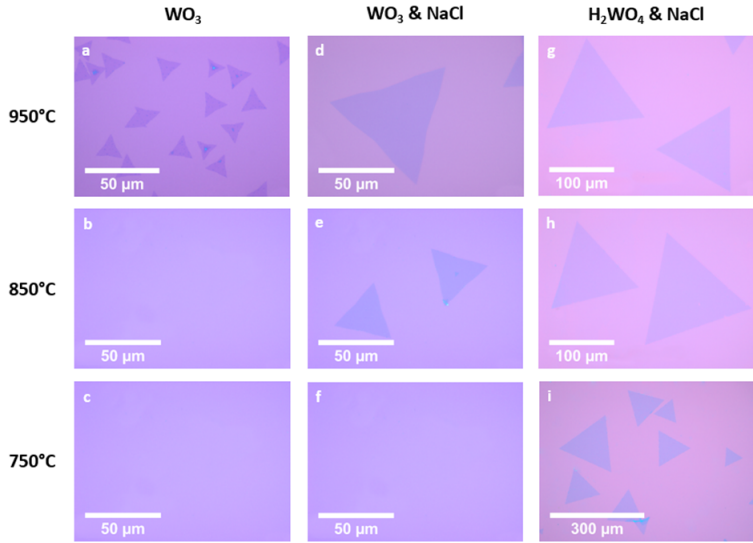


Figure 7: Optical micrographs of  $WS_2$  triangles grown on  $SiO_2/Si$  substrates at different temperatures and using different precursors: (a)  $WO_3$  at 950 °C; (b)  $WO_3$  at 850 °C; (c)  $WO_3$  at 750 °C; (d)  $WO_3 + NaCl$  at 950 °C; (e)  $WO_3 + NaCl$  at 850 °C; (f)  $WO_3 + NaCl$  at 750 °C, the OM appears as a bare  $SiO_2$  substrate; (g)  $H_2WO_4 + NaCl$  at 950 °C; (h)  $H_2WO_4 + NaCl$  at 850 °C; (i)  $H_2WO_4 + NaCl$  at 750 °C.

at temperatures higher than 850 °C and between 50-200  $\mu m$  at 750 °C (Figure 1g,h,i). Continuous polycrystalline monolayer coverage has been obtained over areas of  $\sim 0.8$  mm extension (Figure S2). Increasing the growth pressure (from 1.6 mbar to 13 mbar) at 950 °C bilayered  $WS_2$  flakes are preferentially formed (Figure S3). To understand the facilitated synthesis of  $WS_2$  using  $H_2WO_4$  and  $NaCl$ , we conducted X-ray diffraction (XRD) analysis of the reaction products between  $H_2WO_4+NaCl$  and  $WO_3+NaCl$  systems at different temperatures (500 °C, 650 °C and 750 °C) to understand the chemical differences (Figure S4). We found that the main products of the reactions between  $NaCl$  and  $H_2WO_4$  are:  $NaxWyOz$  and tungsten oxychloride ( $WClO_4$  and  $WO_2Cl_2$ ). The  $NaxWyOz$  possesses a high evaporation temperature as it remains in the crucible (Figure S5) after the synthesis of  $WS_2$  is completed. Further, using this compound as precursors for a new growth of  $WS_2$  at 950 °C did not lead to the formation of any  $WS_2$  flakes, confirming the high evaporation temperature. On the bases of previous studies on the synthesis of bulk crystals, the formation of tungsten oxychloride species ( $WO_2Cl_2$  and/or  $WOCl_4$ ) is likely to occur while the formation of metal halides is less favourable (e.g.  $WCl_6$ ) [ ] [ ]. Tungsten oxychlorides are volatile already at 200 °C [ ] and they can be sulfidized in vapour phase and then be deposited onto the target substrate as atomic clusters.  $WOCl_4$  has been previously used [43] as precursor for the CVD synthesis of  $WS_2$  bulk films. Despite its strong tungsten oxygen double bonds,  $WOCl_4$  proved to be an effective precursor with a clean decomposition pathway in the CVD process without formation of tungsten oxysulfide. We have verified that using this precursor is indeed possible to obtain  $WS_2$  at temperatures as low as 550 °C (Figure S6a). The key role played by the oxyhalide species it becomes apparent if we try to grow  $WS_2$  by using only hydrated tungsten oxide. As this decomposes to form  $WO_3$ , only small  $WS_2$  domains are observed with similar PL characteristics to the  $WO_3$  precursors-growth (Figure S6b). Furthermore, to confirm the key role played by Cl, we replaced  $NaCl$  with  $KCl$  and we obtained comparable growth results (Figure S6c).

The flakes were investigated using HRTEM to confirm high crystallinity of the material (Figure 8). The lattice constant measured in this way has been found to be 0.3 nm, which is consistent with that of 2H-WS<sub>2</sub> (0.318 nm). The AFM characterisation allowed to confirm the presence of monolayer (Figure 8) and bilayer (Figure 17 flakes with the step of 0.8 nm [?][36].

The Raman spectroscopy characterisation of WS<sub>2</sub> flakes obtained under different growth conditions can be seen in Figure 8. All of these spectra exhibit the main 2 peaks at  $\sim(351\pm0.53)$  cm<sup>-1</sup> and  $\sim(417.6\pm1)$  cm<sup>-1</sup>. The latter peak corresponds to the A<sub>1g</sub> vibrational mode while the former peak can be further resolved into two peaks, one related to 2LA vibrational mode and the second to E<sub>2g</sub><sup>1</sup>. As seen in the Figure 21 and Figure 23 the distribution of intensity of both main peaks is uniform across the flakes. Similarly the difference between peak positions of A<sub>1g</sub> and E<sub>2g</sub><sup>1</sup> is also uniformly distributed as seen in Figure 25 and is equal to  $\sim(66.5\pm0.53)$  cm<sup>-1</sup> which is indicative of monolayer [46].

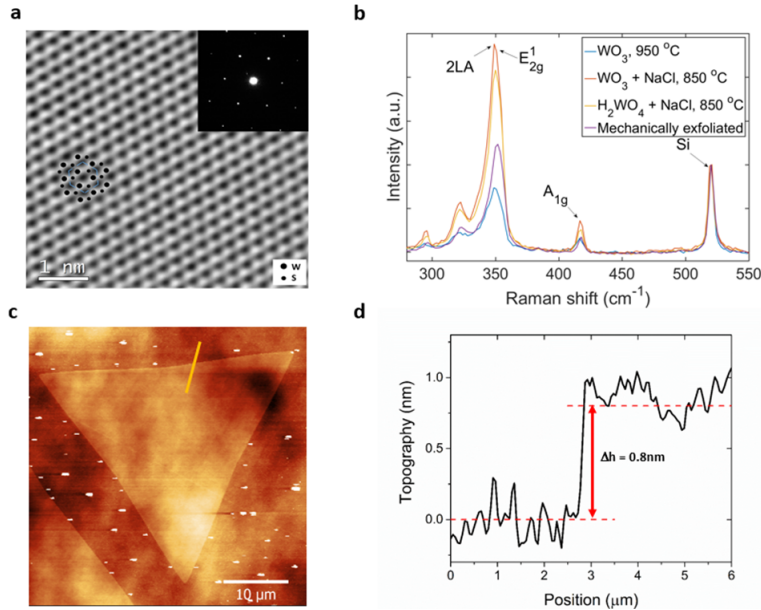


Figure 8: Structural and physical characterization of WS<sub>2</sub> triangles: (a) HRTEM image of the WS<sub>2</sub> lattice grown using  $H_2WO_4 + NaCl$ , the inset report a selected diffraction area which show a hexagonal pattern. (b) Raman spectra showing the characteristics active modes of WS<sub>2</sub> grown under different conditions and compared with mechanically exfoliated flakes. (c) AFM image and (d) corresponding thickness profile of monolayer WS<sub>2</sub>.

As seen in Figure 9 maps of PL intensity has been collected for samples grown using different growth condition. The sample grown using  $WO_3$  at 950 °C appears to be trisected into 3 symmetrical areas. The intensity is lowest along the the trisecting lines and highest in the centre of each of the sub-triangles. The PL peak position is inversely proportional to the intensity of the PL peak as seen in Figure 26. The distribution of the PL peak positions seems to be bimodal with maxima at 1.96 eV and 1.94 eV. The FWHM is distributed mostly uniformly with few small areas of greater and few of smaller FWHM (Figure 27 with the average value of 65 meV. These peak position and FWHM values are comparable with those reported in literature [12][37][14][20]. The PL spectra taken from one of the three smaller parts of the flake are redshifted by about 0.02 eV and are wider than average. This can be explained by the presence of defects, in particular sulfur vacancies, which effectively cause the WS<sub>2</sub> to be n-doped [16][35]. This in turn increases the trion

population which introduces new peak, redshifted by about 30 meV, which results in overall shift and broadening of the PL peak [41][12]. Additionally such localised changes in PL peak intensity and position can be caused by local strain [28][16]. To investigate the potential effect of strain on the observed PL pattern a flake was cut using high power 532nm laser. As seen in Figure 28 the resulting pattern remains the same as before treatment. Therefore the observed pattern is most likely caused by the local variation in defect density [27].

By introducing the NaCl and mixing it with  $WO_3$  precursor  $WS_2$  samples are grown that exhibit higher energy and narrower PL peaks. The spectra are asymmetric and can be therefore deconvoluted to obtain an exciton and trion component (Figure 10). The spatial distribution of the PL position and width is mostly uniform throughout the flake. However the distribution of PL peak positions and FWHM across different flakes grown at the same conditions is bimodal (Figure 10). The PL peak position is found to be ( $\sim 1.95 \pm 0.002$  eV and  $1.96 \pm 0.002$  eV) while the FWHM is ( $\sim 43 \pm 2.8$  meV and  $51 \pm 3$  meV) which is smaller than most reported works [12][37][14][20]. This can be explained by smaller trion component in the PL spectrum which in turn means that  $WS_2$  samples grown at these conditions contain less structural defects compared to the pure  $WO_3$  growth. A difference in growth mechanism (topotactic or molecular conversion) which results in different defect distribution can be attributed to the differences in samples.

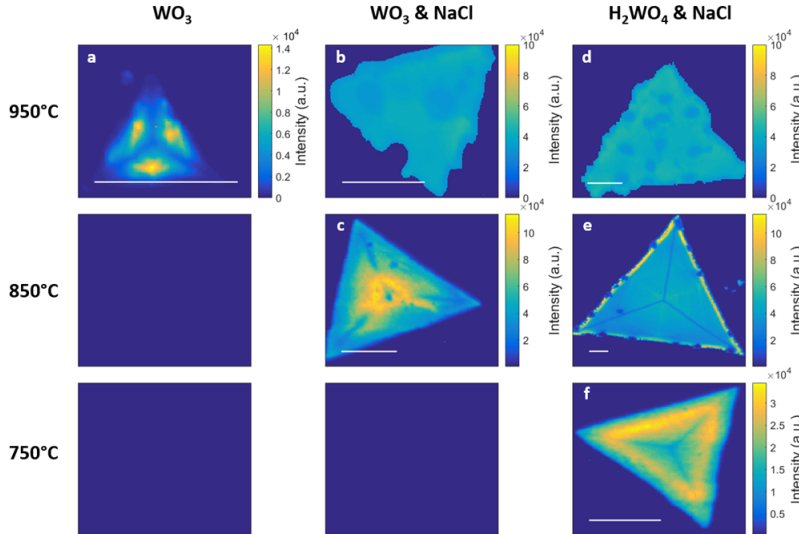


Figure 9: Spatial maps of PL intensity of  $WS_2$  grown in the conditions exemplified in Figure 1. The scale bar length is  $10\mu m$ .

By changing the  $WO_3$  precursor to the  $H_2WO_4$  precursor a further shift in PL peak position, as well as increase in PL intensity and narrowing of the PL peak is observed as seen in Figure 9, 10. The PL peak position distribution across the flake is narrow and is ( $\sim 1.980 \pm 0.005$  eV) which is higher than that of the  $WO_3$  and  $WO_3 + NaCl$  systems. The FWHM is found to be ( $\sim 36 \pm 3$  meV) which is also smaller than that of the  $WO_3$  and  $WO_3 + NaCl$  systems. The PL peak width is also smaller than that reported in literature for CVD grown [12][37][14][20] exfoliated  $WS_2$  [53][38]. At the same time it is comparable to the  $WS_2$  grown on van der Waals substrates [33] as well as mechanically exfoliated  $WS_2$  [18]. Additionally the peak position as well as FWHM variation is also smaller than that of other samples (5meV and 3meV respectively) (Figure 32). The PL peak intensity map (Figure 9) shows that the spatial distribution of intensity is also much more homogeneous with faint weak pattern of three trisecting lines still visible.

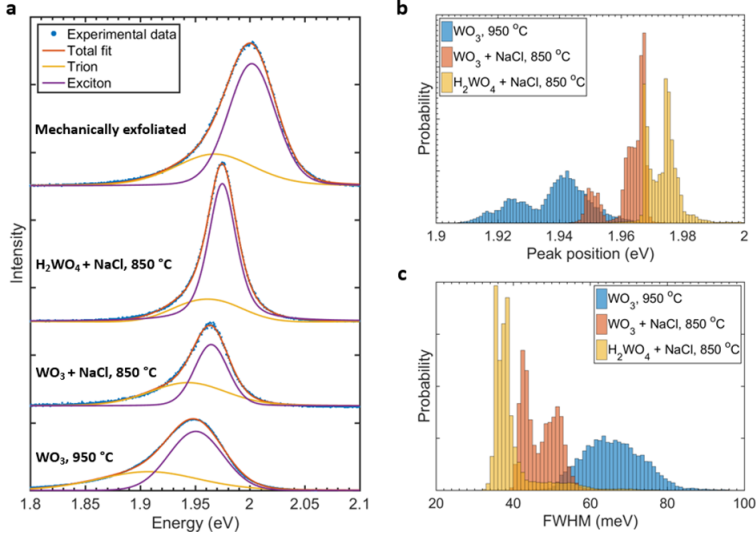


Figure 10: PL spectra characteristics of WS<sub>2</sub> grown using: WO<sub>3</sub> at 950 °C, WO<sub>3</sub>+NaCl at 850 °C, H<sub>2</sub>WO<sub>4</sub>+NaCl at 850 °C: (a) individual spectra (dotted line) and deconvolution in exciton and trion components; (b) distribution of PL peak position and (c) distribution of PL FWHM for several WS<sub>2</sub> grown using the three different precursor systems.

The chemical composition of the flakes grown using  $H_2WO_4 + NaCl$  has been investigated using XPS. The W 4f5/2 and W 4f7/2 core levels show peak positions that of the  $W^{4+}$  in WS<sub>2</sub> [4][32] (32.7 eV 34.8 eV respectively) with FWHM of 1 eV (Figure 11, the smallest possible using Mg K $\alpha$  x-ray source. It means therefore that the WS<sub>2</sub> is of perfect stoichiometric ratio of W and S. Additionally by integrating the intensity of the W 4f and S 2p core level peaks the same result is achieved. Furthermore the S 2p1/2 and 2p3/2 core levels are also present at the expected position for WS<sub>2</sub> (162.3 eV and 163.4 eV respectively, Figure 11) and small FWHM of 1 eV [32]. Small peaks indicative of  $W^{6+}$  (W 4f5/2 and W 4f7/2 at 35.9 eV and 38.1 eV respectively, Figure 11) can be attributed to presence of WO<sub>3</sub> and which partially overlaps with W 5p core level (38.5 eV). These peaks however disappear after the flakes are transferred to another Si/SiO<sub>2</sub> substrate, suggesting that they can be caused by residue WO<sub>3</sub> given that the XPS spot size is relatively big ( $\sim 1$  mm). The FWHM of the W 4f core levels was unchanged after the transfer, indicating that the crystallinity and the quality of the flakes was preserved with no extra defects introduced.

The WS<sub>2</sub> samples grown using WO<sub>3</sub> + NaCl have been characterised by XPS as well and the stoichiometric ratio of 2:1 for S:W has been found. However the  $W^{6+}$  component, caused most likely by presence of WO<sub>3</sub> (W 4f5/2 and W 4f7/2 at 35.9 eV and 38.1 eV respectively) is more pronounced indicating incomplete sulfurisation. Similarly to the sample grown with H<sub>2</sub>WO<sub>4</sub> + NaCl this component disappears entirely upon transferring the sample onto new Si/SiO<sub>2</sub> indicating it is present around the flakes, distributed across the substrate. The  $W^{4+}$  4f core levels peak width is  $\sim 1.2$  eV which indicates higher defect concentration compared to that of the sample grown using H<sub>2</sub>WO<sub>4</sub> + NaCl. This FWHM however increases after the transfer, which is most likely caused by the increase in the concentration of the defects caused by the mechanical stress during the transfer. In conclusion the H<sub>2</sub>WO<sub>4</sub> is shown to be a better precursor compared to WO<sub>3</sub>.

The samples were further characterised for their electrical properties. Bottom-gated field effect transistors were prepared as seen in Figure 12. The FET transfer curve indicates accumulation-type n-channel transistor, where the drain current increases with applied gate bias after a thresh-

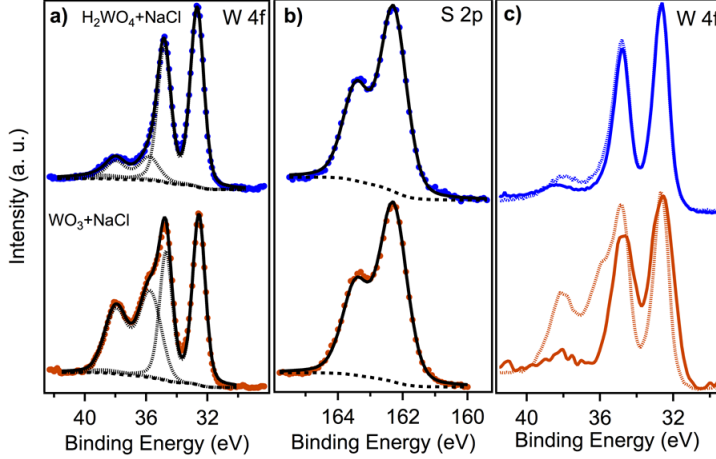


Figure 11: XPS spectra of the W 4f and S 2p core level peak regions. (a) Comparison of W 4f<sub>5/2</sub> , W 4f<sub>7/2</sub> and W 5p core levels of WS<sub>2</sub> grown using H<sub>2</sub>WO<sub>4</sub>+NaCl at 950 °C (blue spectrum) with WS<sub>2</sub> grown using WO<sub>3</sub>+NaCl at 950 °C (red spectrum). The deconvolution of W 4f<sub>5/2</sub> , W 4f<sub>7/2</sub> and W 5p core levels and overall fit of the spectrum are reported as black dashed and a continuous line respectively. (b) The S 2p<sub>1/2</sub> and 2p<sub>3/2</sub> core levels for each of the two growth conditions are reported in the central panel. (c) W 4f<sub>5/2</sub> , W 4f<sub>7/2</sub> and W 5p core levels before (dashed line) and after transfer (continuous like) onto a new SiO<sub>2</sub>/Si substrate are compared showing the complete disappearance of the residual WO<sub>3</sub> components. The spectra were fit by Doniach-Sunjic function after subtracting a Shirley background (black dashed line).

old is crossed. Once the current-bias curve reaches linear range it can be described by  $I_d = \mu_n C_{ox} (W/L)((V_{gs} - V_{th})V_{ds})$ , where  $\mu_n$  is the electron field-effect mobility,  $C_{ox}$  is the oxide dielectric and  $V_{th}$  is the threshold voltage. As seen in Figure 12 a typical response curve for both the as grown as well as transferred samples of WS<sub>2</sub> grown with H<sub>2</sub>WO<sub>4</sub> show an asymmetry around  $V_{ds} = 0$  V due to difference in the source and drain potentials. The Schottky barrier at the source is pinned by the gate, while the barrier at the drain diminishes proportionally to the drain bias and vice versa. The contacts however become more "Ohmic", when the bands bend more at the semiconductor/metal interface while the gate bias increase, leading to more significant tunnelling current.

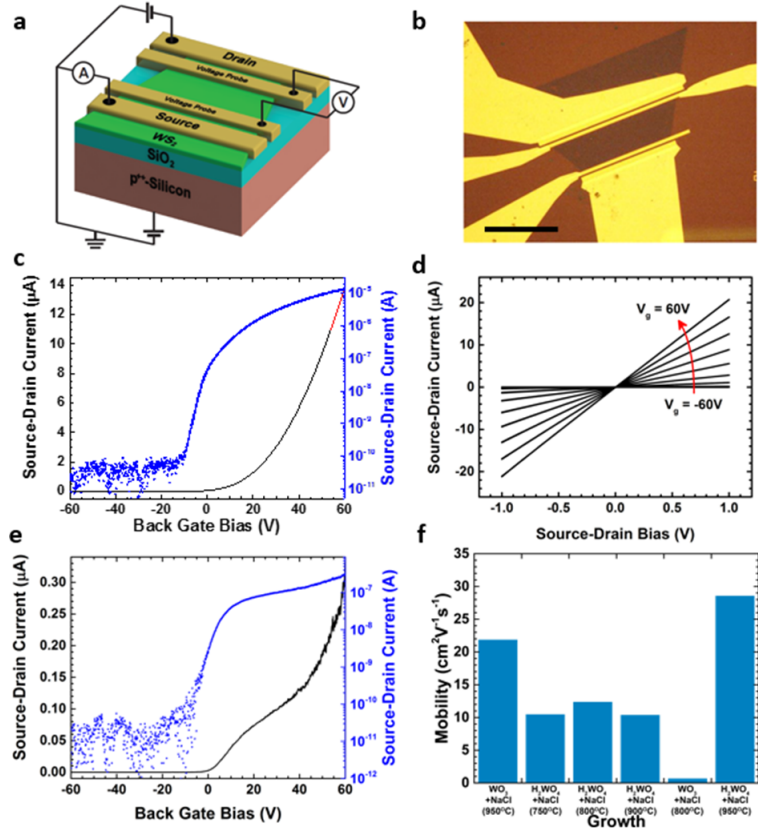


Figure 12: Electrical characteristics of monolayer WS<sub>2</sub>: (a) Schematic of the bottom-gated field effect transistors; (b) optical micrograph of the device (scale bar is  $20\mu\text{m}$ ); (c) FET transfer curve for the monolayer WS<sub>2</sub> grown using H<sub>2</sub>WO<sub>4</sub>+NaCl at  $950\text{ }^{\circ}\text{C}$  showing the highest mobility of  $28\text{ cm}^2/\text{Vs}$  (linear region of the transport graph marked with a red-dashed line); (d) Response curves at different gate biases for a WS<sub>2</sub> triangle grown using H<sub>2</sub>WO<sub>4</sub>+NaCl; (e) FET transfer curve for the monolayer WS<sub>2</sub> grown using WO<sub>3</sub>+NaCl at  $800\text{ }^{\circ}\text{C}$ ; (f) electron mobilities of monolayer WS<sub>2</sub> grown using different conditions.

### 3.3 Conclusions

## 4 Characterisation of WS<sub>2</sub>

### 4.1 Optical microscopy of WS<sub>2</sub> flakes

### 4.2 Raman spectroscopy of WS<sub>2</sub>

#### 4.2.1 Interlayer interactions

#### 4.2.2 Strain

#### 4.2.3 Grain boundaries

### 4.3 Photoluminescence spectroscopy

#### 4.3.1 PL of WS<sub>2</sub> monolayer

#### 4.3.2 PL variation vs flake size

#### 4.3.3 PL variation vs synthesis conditions<sup>5</sup>

#### 4.3.4 Spatial PL variation

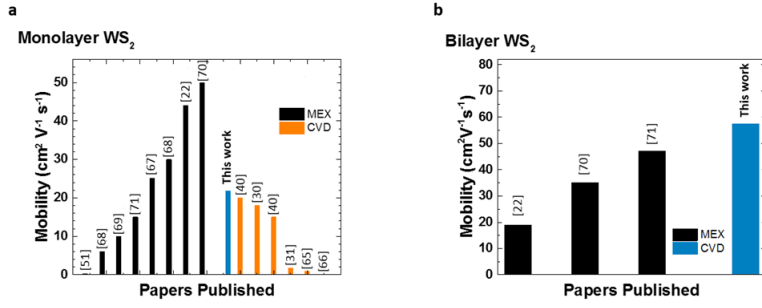


Figure 13: Comparison of our results with the literature of CVD grown material and mechanically exfoliated  $\text{WS}_2$  (MEX) : electron mobility for (a) monolayer  $\text{WS}_2$  and (b) bilayer  $\text{WS}_2$ . The histograms show our record values for both monolayer and bilayer amongst the best values reported for CVD grown  $\text{WS}_2$ .

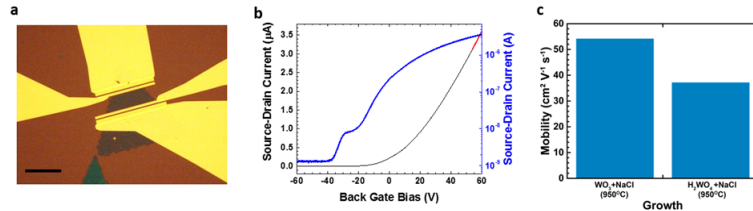


Figure 14: Electrical characteristics of bilayer  $\text{WS}_2$ : (a) Optical micrograph of the device (scale bar is  $30\mu\text{m}$ ); (b) FET transfer curve for the bilayer  $\text{WS}_2$  grown using  $\text{WO}_3 + \text{NaCl}$  at  $950^\circ\text{C}$  showing the highest mobility of  $52 \text{ cm}^2/\text{Vs}$  (linear region of the transport graph marked with a red-dashed line); (c) electron mobility of bilayer  $\text{WS}_2$  grown by using different precursor systems.

F. M. Pesci *et al*, "MoS<sub>2</sub>/WS<sub>2</sub> heterojunction for photoelectrochemical water oxidation", ACS Catalysis, 2017 - accepted

## Conferences

Graphene Week, 13-17 June, 2016. (Best poster)

UK Semiconductors, 14-15 July, 2017.

MRS Boston, 26 November - 1 December, 2017.

## References

- [1] M. Amani, D.-H. Lien, D. Kiriya, J. Xiao, A. Azcatl, J. Noh, S. R. Madhvapathy, R. Adedou, S. KC, M. Dubey, K. Cho, R. M. Wallace, S.-C. Lee, J.-H. He, J. W. Ager, X. Zhang, E. Yablonovitch, and A. Javey. Near-unity photoluminescence quantum yield in MoS<sub>2</sub>. *Science*, 350(6264):1065–1068, nov 2015.

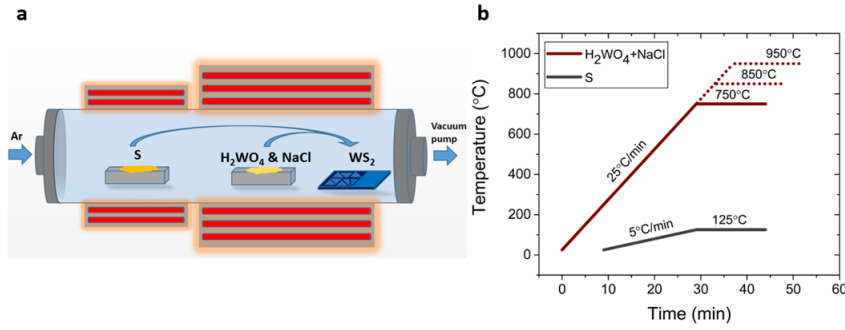


Figure 15: Illustration of: (a) CVD tubular furnace set-up; (b) temperature profile of the sulphur and the W-precursors heaters respectively. The sulphur reaches 125 °C when the metal precursors are at the maximum temperature. The SiO<sub>2</sub>/Si wafers used as substrate for WS<sub>2</sub> growth are placed 1-8 cm downstream the W-precursors crucible and they are subjected to the same temperature.

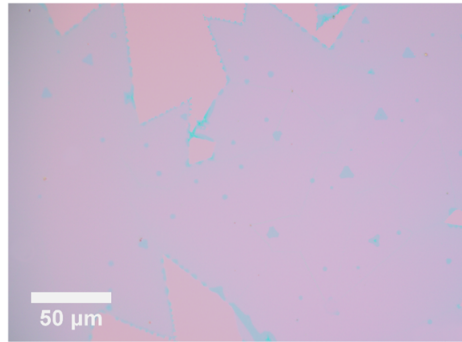


Figure 16: Optical micrograph of a continuous polycrystalline WS<sub>2</sub> monolayer coverage

- [2] Marco Bernardi, Maurizia Palummo, and Jeffrey C. Grossman. Extraordinary sunlight absorption and one nanometer thick photovoltaics using two-dimensional monolayer materials. *Nano Letters*, 13(8):3664–3670, Aug 2013.
- [3] Claire J. Carmalt, Ivan P. Parkin, and Emily S. Peters. Atmospheric pressure chemical vapour deposition of WS<sub>2</sub> thin films on glass. *Polyhedron*, 22(11):1499–1505, jun 2003.
- [4] Mattia Cattelan, Brian Markman, Giacomo Lucchini, Pranab Kumar Das, Ivana Vobornik, Joshua Alexander Robinson, Stefano Agnoli, and Gaetano Granozzi. New strategy for the growth of complex heterostructures based on different 2d materials. *Chemistry of Materials*, 27(11):4105–4113, may 2015.
- [5] Chunxiao Cong, Jingzhi Shang, Xing Wu, Bingchen Cao, Namphung Peimyoo, Caiyu Qiu, Litao Sun, and Ting Yu. Synthesis and optical properties of large-area single-crystalline 2d semiconductor WS<sub>2</sub>monolayer from chemical vapor deposition. *Advanced Optical Materials*, 2(2):131–136, dec 2013.
- [6] Sarah M. Eichfeld, Lorraine Hossain, Yu-Chuan Lin, Aleksander F. Piasecki, Benjamin Kupp, A. Glen Birdwell, Robert A. Burke, Ning Lu, Xin Peng, Jie Li, Angelica Azcatl, Stephen McDonnell, Robert M. Wallace, Moon J. Kim, Theresa S. Mayer, Joan M. Redwing, and

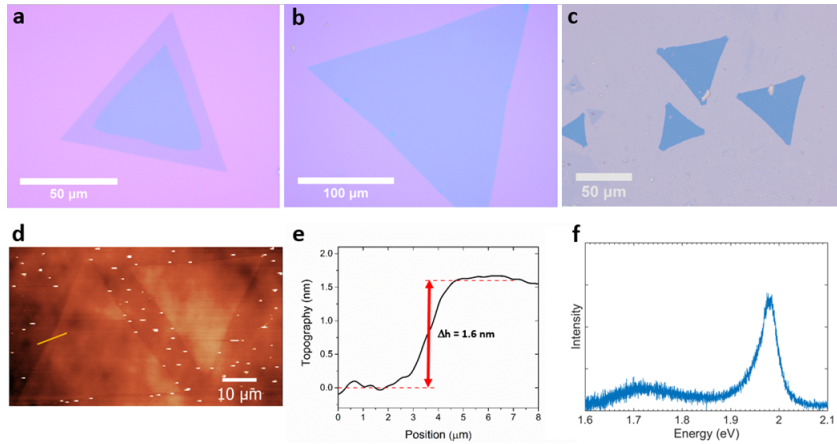


Figure 17: Optical micrographs of (a) second WS<sub>2</sub> layer growing on top of a WS<sub>2</sub> monolayer triangle, (b) uniform bilayer WS<sub>2</sub> triangle, (c) bilayer WS<sub>2</sub> flakes with high nucleation density, AFM (d) image and (e) thickness profile of a bilayer WS<sub>2</sub> triangle, (d) PL spectrum of a bilayer WS<sub>2</sub>.

Joshua A. Robinson. Highly scalable, atomically thin WSe<sub>2</sub> grown via metal–organic chemical vapor deposition. *ACS Nano*, 9(2):2080–2087, feb 2015.

- [7] Ana Laura Elías, Néstor Perea-López, Andrés Castro-Beltrán, Ayse Berkdemir, Ruitao Lv, Simin Feng, Aaron D. Long, Takuya Hayashi, Yoong Ahm Kim, Morinobu Endo, Humberto R. Gutiérrez, Nihar R. Pradhan, Luis Balicas, Thomas E. Mallouk, Florentino López-Urías, Humberto Terrones, and Mauricio Terrones. Controlled synthesis and transfer of large-area ws<sub>2</sub> sheets: From single layer to few layers. *ACS Nano*, 7(6):5235–5242, 2013. PMID: 23647141.
- [8] Qi Fu, Wenhui Wang, Lei Yang, Jian Huang, Jingyu Zhang, and Bin Xiang. Controllable synthesis of high quality monolayer WS<sub>2</sub> on a SiO<sub>2</sub>/si substrate by chemical vapor deposition. *RSC Advances*, 5(21):15795–15799, 2015.
- [9] Yang Gao, Zhibo Liu, Dong-Ming Sun, Le Huang, Lai-Peng Ma, Li-Chang Yin, Teng Ma, Zhiyong Zhang, Xiu-Liang Ma, Lian-Mao Peng, Hui-Ming Cheng, and Wencai Ren. Large-area synthesis of high-quality and uniform monolayer WS<sub>2</sub> on reusable au foils. *Nature Communications*, 6(1), oct 2015.
- [10] Yongji Gong, Junhao Lin, Xingli Wang, Gang Shi, Sidong Lei, Zhong Lin, Xiaolong Zou, Gonglan Ye, Robert Vajtai, Boris I. Yakobson, Humberto Terrones, Mauricio Terrones, Beng Kang Tay, Jun Lou, Sokrates T. Pantelides, Zheng Liu, Wu Zhou, and Pulickel M. Ajayan. Vertical and in-plane heterostructures from WS<sub>2</sub> /MoS<sub>2</sub> monolayers. *Nature Materials*, 13(12):1135–1142, sep 2014.
- [11] Yongji Gong, Zhong Lin, Gonglan Ye, Gang Shi, Simin Feng, Yu Lei, Ana Laura Elías, Nestor Perea-Lopez, Robert Vajtai, Humberto Terrones, Zheng Liu, Mauricio Terrones, and Pulickel M. Ajayan. Tellurium-assisted low-temperature synthesis of MoS<sub>2</sub> and WS<sub>2</sub> monolayers. *ACS Nano*, 9(12):11658–11666, nov 2015.
- [12] Humberto R. Gutiérrez, Nestor Perea-López, Ana Laura Elías, Ayse Berkdemir, Bei Wang, Ruitao Lv, Florentino López-Urías, Vincent H. Crespi, Humberto Terrones, and Mauricio

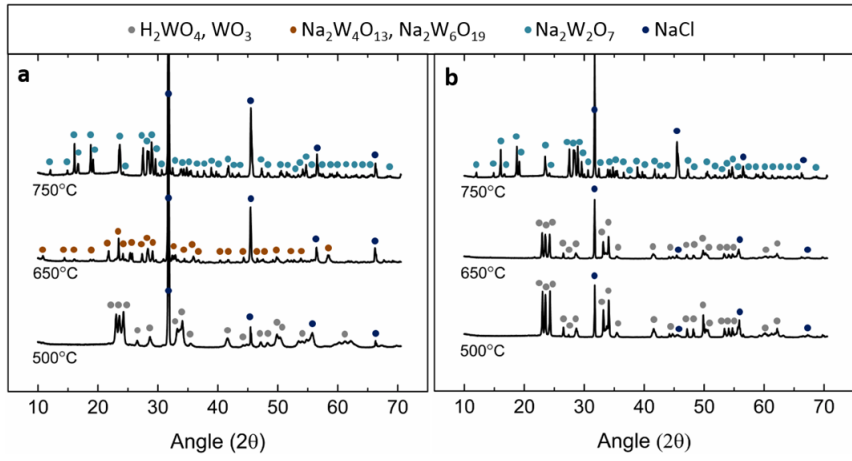


Figure 18: XRD pattern of the residual powder of W-preursors after thermal treatment at 500 °C, 650 °C and 750 °C respectively, using (a)  $\text{H}_2\text{WO}_4 + \text{NaCl}$  and (b)  $\text{WO}_3 + \text{NaCl}$  as precursor.

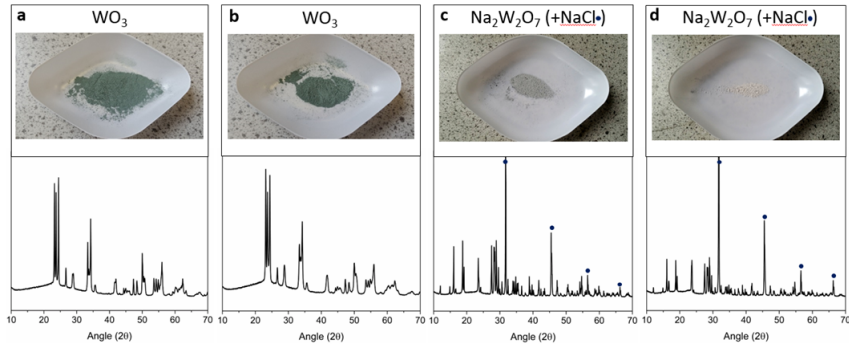


Figure 19: Residual powders of the W-preursors and their XRD patterns after thermal treatment at 750°C using (a)  $\text{WO}_3$ , (b)  $\text{H}_2\text{WO}_4$ , (c)  $\text{WO}_3 + \text{NaCl}$ , and (d)  $\text{H}_2\text{WO}_4 + \text{NaCl}$  as precursor. The blue dots in the XRD patterns indicate the presence of residual NaCl.

Terrones. Extraordinary room-temperature photoluminescence in triangular ws2 monolayers. *Nano Letters*, 13(8):3447–3454, dec 2013. PMID: 23194096.

- [13] Wolfgang K. Hofmann. Thin films of molybdenum and tungsten disulphides by metal organic chemical vapour deposition. *Journal of Materials Science*, 23(11):3981–3986, nov 1988.
- [14] Peng Hu, Jun Ye, Xuexia He, Kezhao Du, Keke K. Zhang, Xingzhi Wang, Qihua Xiong, Zheng Liu, Hui Jiang, and Christian Kloc. Control of radiative exciton recombination by charge transfer induced surface dipoles in MoS<sub>2</sub> and WS<sub>2</sub> monolayers. *Scientific Reports*, 6(1), apr 2016.
- [15] Wang Yao Di Xiao Hualing Zeng, Junfeng Dai and Xiaodong Cui. Valley polarization in mos<sub>2</sub> monolayers by optical pumping. *Nature Nanotechnology*, 7(8):490–493, jun 2012.
- [16] Yeung Yu Hui, Xiaofei Liu, Wenjing Jie, Ngai Yui Chan, Jianhua Hao, Yu-Te Hsu, Lain-Jong Li, Wanlin Guo, and Shu Ping Lau. Exceptional tunability of band energy in a compressively strained trilayer MoS<sub>2</sub> sheet. *ACS Nano*, 7(8):7126–7131, jul 2013.

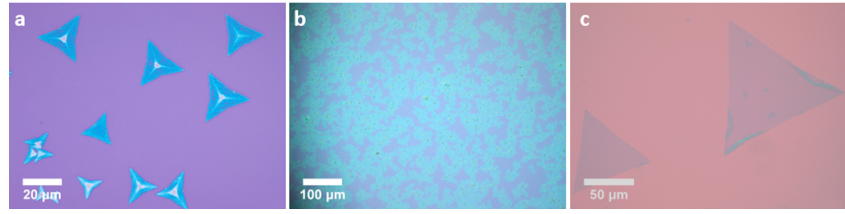


Figure 20: Optical micrographs of WS<sub>2</sub> triangles and amorphous domains grown on SiO<sub>2</sub>/Si substrates by using (a) WOCl<sub>4</sub> at 600°C, (b) only H<sub>2</sub>WO<sub>4</sub> at 850°C, (c) H<sub>2</sub>WO<sub>4</sub>+KCl at 850°C.

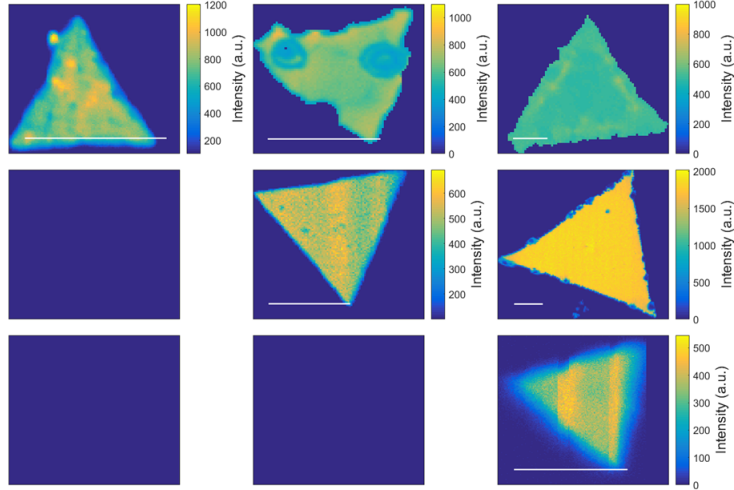


Figure 21: Raman spectroscopy:  $2LA + E_{2g}^1$  peak intensity. Scale bar 10  $\mu$ m

- [17] M Waqas Iqbal, M Zahir Iqbal, M Farooq Khan, M Arslan Shehzad, Yongho Seo, Jong Hyun Park, Chanyong Hwang, and Jonghwa Eom. High-mobility and air-stable single-layer WS<sub>2</sub> field-effect transistors sandwiched between chemical vapor deposition-grown hexagonal BN films. *Scientific Reports*, 5(1), jun 2015.
- [18] Sanghyun Jo, Nicolas Ubrig, Helmuth Berger, Alexey B. Kuzmenko, and Alberto F. Morpurgo. Mono- and bilayer ws<sub>2</sub> light-emitting transistors. *Nano Letters*, 14(4):2019–2025, 2014. PMID: 24669957.
- [19] Kibum Kang, Saien Xie, Lujie Huang, Yimo Han, Pinshane Y. Huang, Kin Fai Mak, Cheol-Joo Kim, David Muller, and Jiwoong Park. High-mobility three-atom-thick semiconducting films with wafer-scale homogeneity. *Nature*, 520(7549):656–660, apr 2015.
- [20] Kyung Nam Kang, Kyle Godin, and Eui-Hyeok Yang. The growth scale and kinetics of WS<sub>2</sub> monolayers under varying h<sub>2</sub> concentration. *Scientific Reports*, 5(1), aug 2015.
- [21] A. Kuc, N. Zibouche, and T. Heine. Influence of quantum confinement on the electronic structure of the transition metal sulfide  $ts_2$ . *Phys. Rev. B*, 83(24):245213, Jun 2011.
- [22] Yi-Hsien Lee, Lili Yu, Han Wang, Wenjing Fang, Xi Ling, Yumeng Shi, Cheng-Te Lin, Jing-Kai Huang, Mu-Tung Chang, Chia-Seng Chang, Mildred Dresselhaus, Tomas Palacios, Lain-Jong

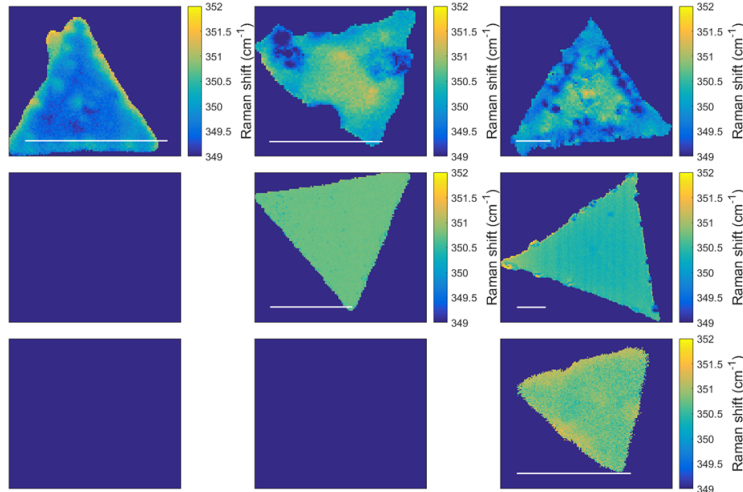


Figure 22: Raman spectroscopy:  $2LA + E_{2g}^1$  peak position. Scale bar is  $10 \mu\text{m}$

Li, and Jing Kong. Synthesis and transfer of single-layer transition metal disulfides on diverse surfaces. *Nano Letters*, 13(4):1852–1857, mar 2013.

- [23] Shisheng Li, Shunfeng Wang, Dai-Ming Tang, Weijie Zhao, Huilong Xu, Leiqiang Chu, Yoshio Bando, Dmitri Golberg, and Goki Eda. Halide-assisted atmospheric pressure growth of large WSe<sub>2</sub> and WS<sub>2</sub> monolayer crystals. *Applied Materials Today*, 1(1):60–66, nov 2015.
- [24] Tianshu Li and Giulia Galli. Electronic properties of mos<sub>2</sub> nanoparticles. *The Journal of Physical Chemistry C*, 111(44):16192–16196, nov 2007.
- [25] Yilei Li, Yi Rao, Kin Fai Mak, Yumeng You, Shuyuan Wang, Cory R. Dean, and Tony F. Heinz. Probing symmetry properties of few-layer mos<sub>2</sub> and h-bn by optical second-harmonic generation. *Nano Letters*, 13(7):3329–3333, jun 2013. PMID: 23718906.
- [26] Liangxu Lin, Yaixian Xu, Shaowei Zhang, Ian M. Ross, Albert C. M. Ong, and Dan A. Allwood. Fabrication of luminescent monolayered tungsten dichalcogenides quantum dots with giant spin-valley coupling. *ACS Nano*, 7(9):8214–8223, 2013. PMID: 23968363.
- [27] Hongwei Liu, Junpeng Lu, Kenneth Ho, Zhenliang Hu, Zhiya Dang, Alexandra Carvalho, Hui Ru Tan, Eng Soon Tok, and Chorng Haur Sow. Fluorescence concentric triangles: A case of chemical heterogeneity in WS<sub>2</sub> atomic monolayer. *Nano Letters*, 16(9):5559–5567, aug 2016.
- [28] Zheng Liu, Matin Amani, Sina Najmaei, Quan Xu, Xiaolong Zou, Wu Zhou, Ting Yu, Caiyu Qiu, A. Glen Birdwell, Frank J. Crowne, Robert Vajtai, Boris I. Yakobson, Zhenhai Xia, Madan Dubey, Pulickel M. Ajayan, and Jun Lou. Strain and structure heterogeneity in MoS<sub>2</sub> atomic layers grown by chemical vapour deposition. *Nature Communications*, 5(1), nov 2014.
- [29] He Keliang Lee Changgu Lee Gwan Hyoung Hone James Heinz Tony F. Mak, Kin Fai and Jie Shan. Tightly bound trions in monolayer. *Nature Materials*, 12(3):207–211, dec 2013.

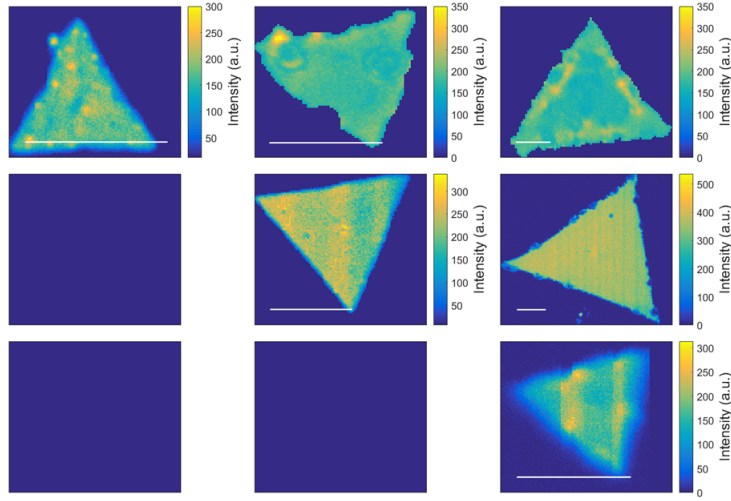


Figure 23: Raman spectroscopy:  $A_{1g}$  peak intensity. Scale bar is  $10 \mu\text{m}$

- [30] He Keliang Shan Jie Mak, Kin Fai and Tony F. Heinz. Control of valley polarization in monolayer mos<sub>2</sub> by optical helicity. *Nature Nanotechnology*, 7(8):494–498, jun 2012.
- [31] Kin Fai Mak, Changgu Lee, James Hone, Jie Shan, and Tony F. Heinz. Atomically thin mos<sub>2</sub>: A new direct-gap semiconductor. *Phys. Rev. Lett.*, 105(13):136805, Sep 2010.
- [32] H. Martinez, A. Benayad, D. Gonbeau, P. Vinatier, B. Pecquenard, and A. Levasseur. Influence of the cation nature of high sulfur content oxysulfide thin films MOySz (m=w, ti) studied by XPS. *Applied Surface Science*, 236(1-4):377–386, sep 2004.
- [33] Mitsuhiro Okada, Takumi Sawazaki, Kenji Watanabe, Takashi Taniguchi, Hiroki Hibino, Hisanori Shinohara, and Ryo Kitaura. Direct chemical vapor deposition growth of ws<sub>2</sub> atomic layers on hexagonal boron nitride. *ACS Nano*, 8(8):8273–8277, 2014. PMID: 25093606.
- [34] Namphung Peimyoo, Jingzhi Shang, Chunxiao Cong, Xiaonan Shen, Xiangyang Wu, Edwin K. L. Yeow, and Ting Yu. Nonblinking, intense two-dimensional light emitter: Monolayer ws<sub>2</sub> triangles. *ACS Nano*, 7(12):10985–10994, 2013. PMID: 24266716.
- [35] Namphung Peimyoo, Weihuang Yang, Jingzhi Shang, Xiaonan Shen, Yanlong Wang, and Ting Yu. Chemically driven tunable light emission of charged and neutral excitons in monolayer WS<sub>2</sub>. *ACS Nano*, 8(11):11320–11329, oct 2014.
- [36] Filip A. Rasmussen and Kristian S. Thygesen. Computational 2d materials database: Electronic structure of transition-metal dichalcogenides and oxides. *The Journal of Physical Chemistry C*, 119(23):13169–13183, jun 2015.
- [37] Youmin Rong, Ye Fan, Ai Leen Koh, Alex W. Robertson, Kuang He, Shanshan Wang, Haijie Tan, Robert Sinclair, and Jamie H. Warner. Controlling sulphur precursor addition for large single crystal domains of WS<sub>2</sub>. *Nanoscale*, 6(20):12096–12103, sep 2014.

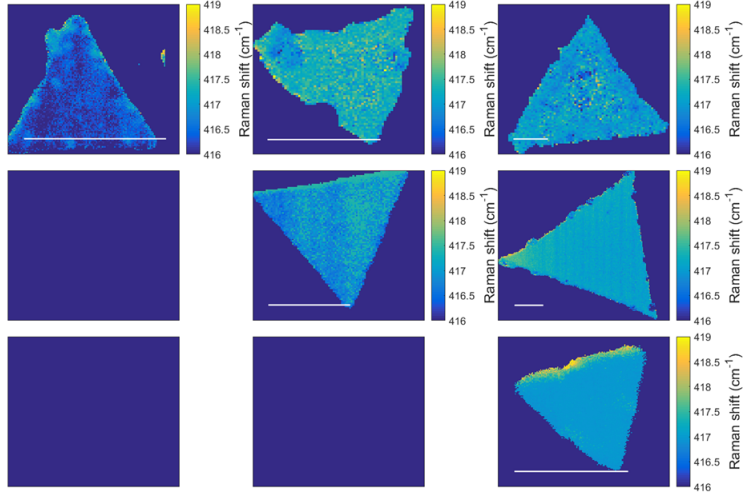


Figure 24: Raman spectroscopy:  $A_{1g}$  peak position. Scale bar is  $10 \mu\text{m}$

- [38] Jingzhi Shang, Xiaonan Shen, Chunxiao Cong, Namphung Peimyoo, Bingchen Cao, Mustafa Eginligil, and Ting Yu. Observation of excitonic fine structure in a 2d transition-metal dichalcogenide semiconductor. *ACS Nano*, 9(1):647–655, 2015. PMID: 25560634.
- [39] Andrea Splendiani, Liang Sun, Yuanbo Zhang, Tianshu Li, Jonghwan Kim, Chi-Yung Chim, Giulia Galli, and Feng Wang. Emerging photoluminescence in monolayer mos<sub>2</sub>. *Nano Letters*, 10(4):1271–1275, apr 2010. PMID: 20229981.
- [40] Xiaona Liu Pingheng Tan Tengfei Yan, Xiaofen Qiao and Xinhui Zhang. Photoluminescence properties and exciton dynamics in monolayer wse<sub>2</sub>. *Applied Physics Letters*, 105(10):101901, sep 2014.
- [41] Sefaattin Tongay, Joonki Suh, Can Ataca, Wen Fan, Alexander Luce, Jeong Seuk Kang, Jonathan Liu, Changhyun Ko, Rajamani Raghunathanan, Jian Zhou, Frank Ogletree, Jingbo Li, Jeffrey C. Grossman, and Junqiao Wu. Defects activated photoluminescence in two-dimensional semiconductors: interplay between bound, charged and free excitons. *Scientific Reports*, 3(1), sep 2013.
- [42] Qing Hua Wang, Kourosh Kalantar-Zadeh, Andras Kis, Jonathan N. Coleman, and Michael S. Strano. Electronics and optoelectronics of two-dimensional transition metal dichalcogenides. *Nature Nanotechnology*, 7:699 EP –, Nov 2012. Review Article.
- [43] Kiran Kumar Amara Jing Ren Pang Minglin Toh Xin Zhang Christian Kloc Ping Heng Tane Weijie Zhao, Zohreh Ghorannevis and Goki Eda. Lattice dynamics in mono- and few-layer sheets of ws<sub>2</sub> and wse<sub>2</sub>. *Nanoscale*, 5(20):9677–9683, August 2013.
- [44] J.A. Wilson and A.D. Yoffe. The transition metal dichalcogenides discussion and interpretation of the observed optical, electrical and structural properties. *Advances in Physics*, 18(73):193–335, may 1969.
- [45] F. Withers, O. Del Pozo-Zamudio, A. Mishchenko, A. P. Rooney, A. Gholinia, K. Watanabe, T. Taniguchi, S. J. Haigh, A. K. Geim, A. I. Tartakovskii, and K. S. Novoselov. Light-emitting

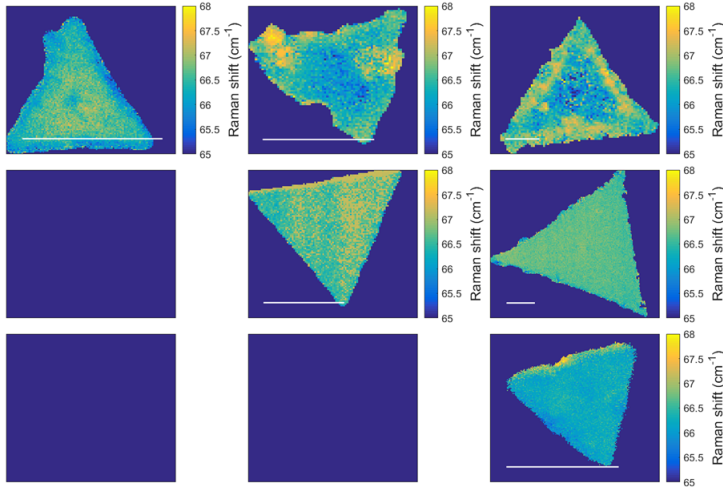


Figure 25: Raman spectroscopy:  $2LA - A_{1g}$  energy differences. Scale bar is  $10 \mu\text{m}$

diodes by band-structure engineering in van der waals heterostructures. *Nature Materials*, 14(3):301–306, feb 2015.

- [46] Freddie Withers, Thomas Hardisty Bointon, David Christopher Hudson, Monica Felicia Craciun, and Saverio Russo. Electron transport of WS<sub>2</sub> transistors in a hexagonal boron nitride dielectric environment. *Scientific Reports*, 4(1), may 2014.
- [47] Di Xiao, Gui-Bin Liu, Wanxiang Feng, Xiaodong Xu, and Wang Yao. Coupled spin and valley physics in monolayers of *mos*<sub>2</sub> and other group-vi dichalcogenides. *Phys. Rev. Lett.*, 108(19):196802, May 2012.
- [48] Zai-Quan Xu, Yupeng Zhang, Shenghuang Lin, Changxi Zheng, Yu Lin Zhong, Xue Xia, Zhipeng Li, Ponraj Joice Sophia, Michael S. Fuhrer, Yi-Bing Cheng, and Qiaoliang Bao. Synthesis and transfer of large-area monolayer ws<sub>2</sub> crystals: Moving toward the recyclable use of sapphire substrates. *ACS Nano*, 9(6):6178–6187, 2015. PMID: 25961515.
- [49] Long Yuan and Libai Huang. Exciton dynamics and annihilation in WS<sub>2</sub> 2d semiconductors. *Nanoscale*, 7(16):7402–7408, 2015.
- [50] Seok Joon Yun, Sang Hoon Chae, Hyun Kim, Jin Cheol Park, Ji-Hoon Park, Gang Hee Han, Joo Song Lee, Soo Min Kim, Hye Min Oh, Jinbong Seok, Mun Seok Jeong, Ki Kang Kim, and Young Hee Lee. Synthesis of centimeter-scale monolayer tungsten disulfide film on gold foils. *ACS Nano*, 9(5):5510–5519, apr 2015.
- [51] Longhui Zeng, Lili Tao, Chunyin Tang, Bo Zhou, Hui Long, Yang Chai, Shu Ping Lau, and Yuen Hong Tsang. High-responsivity UV-vis photodetector based on transferable WS<sub>2</sub> film deposited by magnetron sputtering. *Scientific Reports*, 6(1), jan 2016.
- [52] Yu Zhang, Yanfeng Zhang, Qingqing Ji, Jing Ju, Hongtao Yuan, Jianping Shi, Teng Gao, Donglin Ma, Mengxi Liu, Yubin Chen, Xiuju Song, Harold Y. Hwang, Yi Cui, and Zhongfan Liu. Controlled growth of high-quality monolayer ws<sub>2</sub> layers on sapphire and imaging its grain boundary. *ACS Nano*, 7(10):8963–8971, 2013. PMID: 24047054.

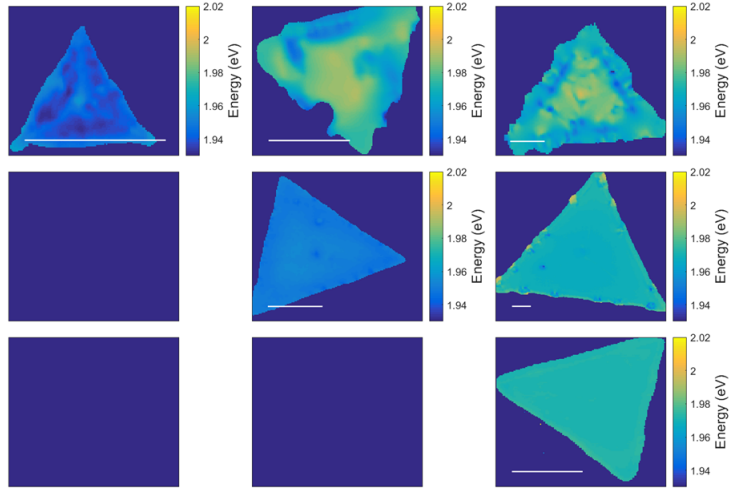


Figure 26: PL spectroscopy: PL peak position. Scale bar is  $10 \mu\text{m}$

- [53] Weijie Zhao, Zohreh Ghorannevis, Leiqiang Chu, Minglin Toh, Christian Kloc, Ping-Heng Tan, and Goki Eda. Evolution of electronic structure in atomically thin sheets of ws<sub>2</sub> and wse<sub>2</sub>. *ACS Nano*, 7(1):791–797, dec 2013. PMID: 23256505.
- [54] Z. Y. Zhu, Y. C. Cheng, and U. Schwingenschlögl. Giant spin-orbit-induced spin splitting in two-dimensional transition-metal dichalcogenide semiconductors. *Phys. Rev. B*, 84(15):153402, Oct 2011.

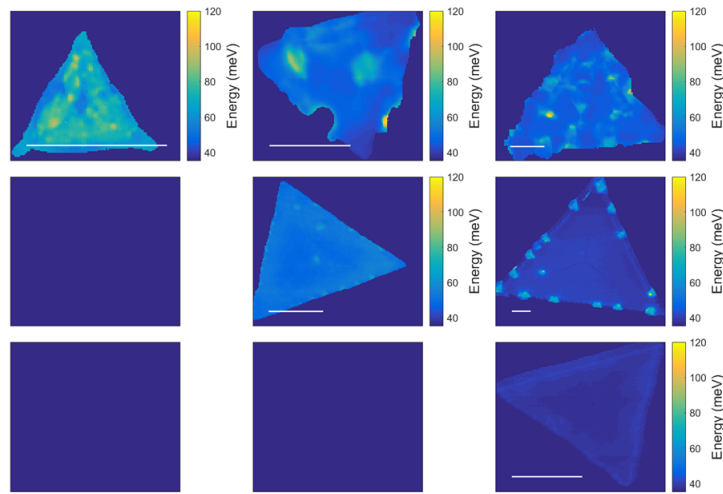


Figure 27: PL spectroscopy: PL FWHM. Scale bar is  $10 \mu\text{m}$

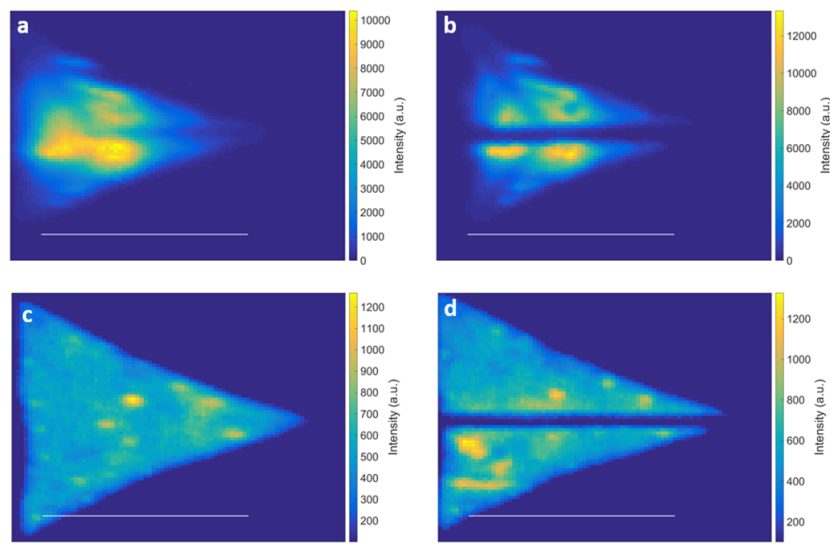


Figure 28: PL intensity (a) before and (b) after the cutting.  $2LA + E_{2g}^1$  Raman intensity (c) before and (d) after the cutting. Scale bar is  $10 \mu\text{m}$

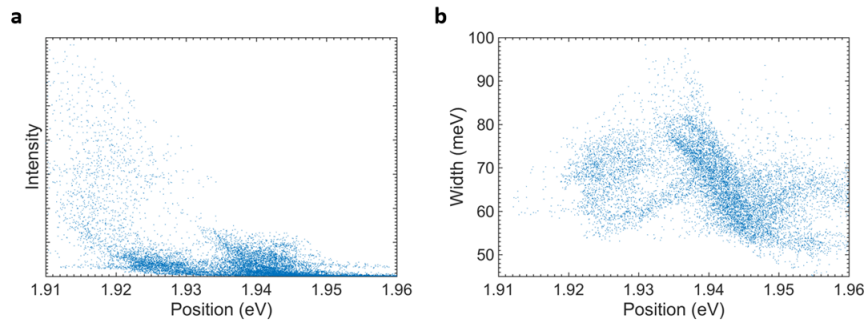


Figure 29: (a) PL Intensity vs position, (b) PL FWHM vs position of  $WS_2$  grown using  $WO_3$  at  $950\text{ }^\circ\text{C}$

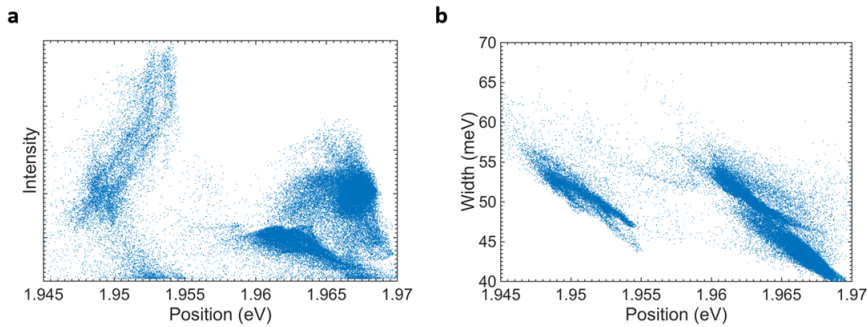


Figure 30: PL Intensity vs position, (b) PL FWHM vs position of  $WS_2$  grown using  $WO_3 + NaCl$  at  $850\text{ }^\circ\text{C}$

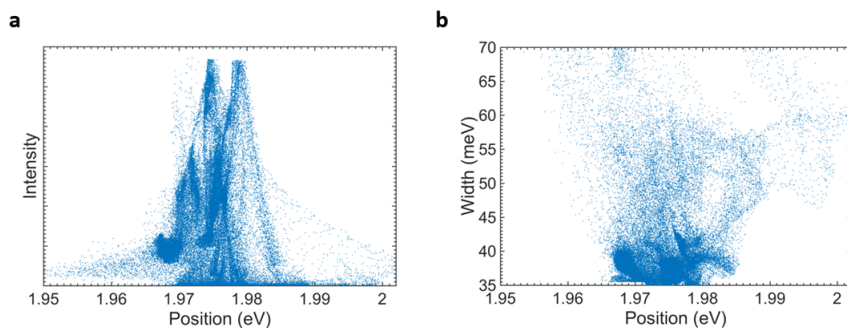


Figure 31: (a) PL Intensity vs position, (b) PL FWHM vs position of  $WS_2$  grown using  $H_2WO_4 + NaCl$  at  $850\text{ }^\circ\text{C}$

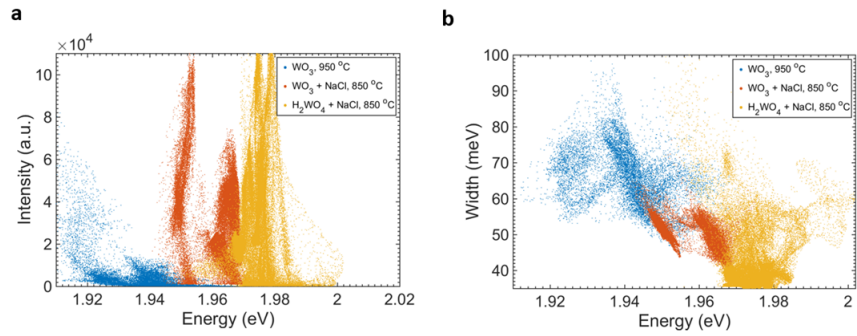


Figure 32: (a) PL Intensity vs position, (b) PL FWHM vs position of  $WS_2$  grown using  $WO_3$ ,  $WO_3 + NaCl$ ,  $H_2WO_4 + NaCl$